Monthly Notices of the ROYAL ASTRONOMICAL SOCIETY

MNRAS **521,** L53–L58 (2023) https://doi.org/10.1093/mnrasl/slad023

Flaring activity from magnetic reconnection in BL Lacertae

S. Agarwal [1]★ B. Banerjee [2,3] A. Shukla,[1] J. Roy [4] S. Acharya [1,5] B. Vaidya [1] V. R. Chitnis,[6] S. M. Wagner [7] K. Mannheim[7] and M. Branchesi[2,3]

[1]*Department of Astronomy, Astrophysics and Space Engineering, Indian Institute of Technology Indore, Khandwa Road, Simrol, Indore 453552, Madhya Pradesh, India*
[2]*Gran Sasso Science Institute, Viale F. Crispi 7, I-67100 L'Aquila (AQ), Italy*
[3]*INFN – Laboratori Nazionali del Gran Sasso, I-67100 L'Aquila (AQ), Italy*
[4]*Inter-University Centre for Astronomy and Astrophysics, Pune 411007, Maharashtra, India*
[5]*Hamburger Sternwarte, Universität Hamburg, Gojenbergsweg 112, D-21029 Hamburg, Germany*
[6]*Tata Institute of Fundamental Research, Homi Bhabha Road, Colaba, Mumbai 400005, Maharashtra, India*
[7]*Julius-Maximilians-Universität Würzburg, Fakultät für Physik und Astronomie, Institut für Theoretische Physik und Astrophysik, Lehrstuhl für Astronomie, Emil-Fischer Str 31, D-97074 Würzburg, Germany*

Accepted 2023 February 13. Received 2023 February 12; in original form 2022 September 21

ABSTRACT

The evolution of the spectral energy distribution during flares constrains models of particle acceleration in blazar jets. The archetypical blazar BL Lacertae provided a unique opportunity to study spectral variations during an extended strong flaring episode from 2020 to 2021. During its brightest γ-ray state, the observed flux (0.1–300 GeV) reached up to 2.15×10^{-5} ph cm^{-2} s^{-1}, with sub-hour-scale variability. The synchrotron hump extended into the X-ray regime showing a minute-scale flare with an associated peak shift of inverse-Compton hump in γ-rays. In shock acceleration models, a high Doppler factor value >100 is required to explain the observed rapid variability, change of state, and γ-ray peak shift. Assuming particle acceleration in minijets produced by magnetic reconnection during flares, on the other hand, alleviates the constraint on required bulk Doppler factor. In such jet-in-jet models, observed spectral shift to higher energies (towards TeV regime) and simultaneous rapid variability arises from the accidental alignment of a magnetic plasmoid with the direction of the line of sight. We infer a magnetic field of $\sim$0.6 G in a reconnection region located at the edge of broad-line region ($\sim$0.02 pc). The scenario is further supported by lognormal flux distribution arising from merging of plasmoids in reconnection region.

Key words: magnetic reconnection – radiation mechanisms: non-thermal – BL Lacertae objects: individual: BL Lac – galaxies: jets – gamma-rays: galaxies – X-rays: galaxies.

1 INTRODUCTION

The BL Lacertae (BL Lac) is an eponymous blazar at a redshift of 0.069 (Miller, French & Hawley 1978) that is usually classified as low-peaked BL Lac (Nilsson et al. 2018) with an intermediate BL Lac behaviour at times (Ackermann et al. 2011). A peculiar property of the source is the detection of weak Hα and Hβ lines underscoring the presence of a feeble broad-line region (BLR) in spite of its classification in the BL Lac class (Corbett et al. 1996). Multiwavelength (MWL) studies in flaring and quiescent states require a dominant component of γ-ray emission from the inverse-Compton (IC) upscattering of external seed photons (Abdo et al. 2011). Thus, there is a high probability that the BLR serves as a source of seed photons for the electron population in the jets. Emitted high-energy (HE) photons are expected to be absorbed and attenuated by the ultraviolet (UV) photons emitted by the BLR and produce a curvature in the HE γ-ray spectrum (Poutanen & Stern 2010). Interestingly, the source is a known TeV emitter and has been observed in very high energy (VHE; $E > 30$ GeV) γ-rays by Major Atmospheric Gamma Imaging Cherenkov Telescope (MAGIC) and Very Energetic Radiation Imaging Telescope Array System (VERITAS) (Arlen et al. 2013; Abeysekara et al. 2018; MAGIC Collaboration 2019). The observed fast TeV variability can be interpreted as a small emission zone close to the black hole magnetosphere (Aleksić et al. 2014), mini jet-in-jet interaction from magnetic reconnection (Giannios, Uzdensky & Begelman 2009), star–jet interaction (Banasiński, Bednarek & Sitarek 2016), or a two-zone emission region (Tavecchio et al. 2011) consisting of a small blob with a large Doppler factor interacting with a larger emission region. In this work, we strive to elucidate the possible physical processes supporting observed state change in BL Lac during the enhanced activity period. The flow of the letter will be as follows: Sections 2 and 3 present the data reduction and techniques used in analysis, respectively. Sections 4 and 5 cover the results and discussion, respectively.

2 DATA ACQUISITION AND ANALYSIS

The *Fermi* Large Area Telescope (LAT) is a pair-conversion HE γ-ray (0.1–300 GeV) telescope onboard the *Fermi* spacecraft. Fermi Science tools and open source FERMIPY package (Wood et al. 2017) are used to analyse source data using the latest instrument response function `P8R3_SOURCE_V3`. A circular 15° region of interest is

★ E-mail: sush.agarwal16@gmail.com

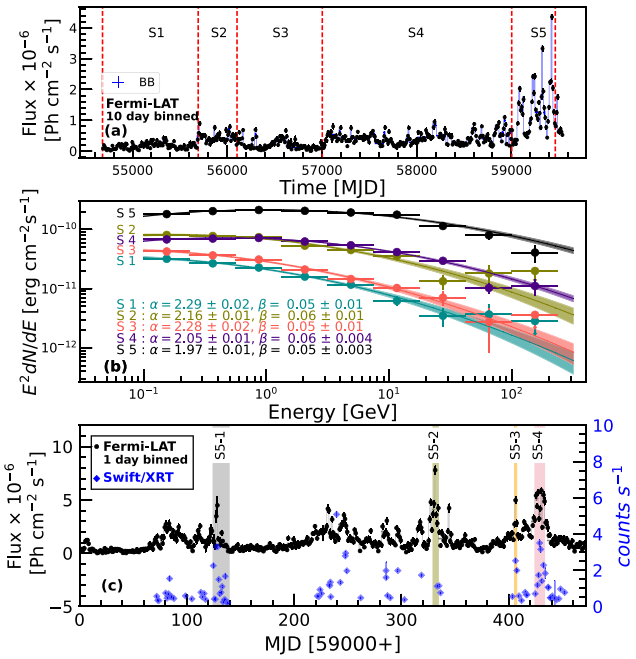

Figure 1. (a) The *Fermi*-LAT LCs of BL Lac for MJD 54683–59473. The red lines categorize 13 yr of data into five flux states (S1–S5). (b) The HE (0.1–300 GeV) spectrum of the five states. (c) The 1 d binned *Fermi*-LAT LC of BL Lac for MJD 59000–59478 (S5). The highlighted regions in grey, olive, orange, and pink represent the periods under study (S5-1, S5-2, S5-3, and S5-4). Bayesian blocks on top highlight the variable nature of the LC. *Swift*-XRT overall binned LC for MJD 59000–59478 is plotted (in blue).

considered around the source. Shukla & Mannheim (2020) provide details on the LAT data reduction procedure followed in this work.

We analysed 33 *Swift* X-Ray Telescope (XRT) pointed source observations on four time segments corresponding to *Fermi* flaring episodes (Fig. 1c). Data reduction to generate light curves, spectrum, ancillary response file, and redistribution matrix file is done using version 1.0.2 of the calibration data base and version 6.29 of the HEASOFT software for the Photon Counting and Window Timing modes data. The data are corrected for the pile-up using the procedures given in website (https://www.swift.ac.uk/analysis/xrt/pileup.php). An annular source region with an outer radius of 30 arcsec and background region files were extracted farther away from the source using a circular region of radius 50 arcsec. The background-subtracted spectrum was modelled with an absorbed power law (PL) using photoelectric absorption model `tbabs` in XSPEC with a fixed galactic absorption hydrogen column density of $N_{\rm H} = 2.70 \times 10^{21}$ cm^{-2} (D'Ammando 2021) in the source direction. The X-ray flux count rate in Figs 1(c) and 2 are from the preliminary analysis of the *Swift*-XRT data (Stroh & Falcone 2013).

We use simultaneous *Swift*- Ultraviolet Optical Telescope (UVOT) observations in all six filters for optical and UV coverage: *V* (500–600 nm), *B* (380–500 nm), *U* (300–400 nm), *W1* (220–400 nm), *M2* (200–280 nm), and *W2* (180–260 nm).Source counts are extracted from a circle of 5 arcsec radius centred on the source coordinates. Background counts are derived from a 20 arcsec radius circular region in a nearby source-free region (D'Ammando 2021). Magnitude and flux are extracted from the generated source and background region files. The flux densities for host galaxy in *v*, *b*, *u*, *w1*, *m2*, and *w2* bands are taken to be 2.89, 1.30, 0.36, 0.026, 0.020, and 0.017 mJy following Raiteri et al. (2013) and subtracted. The host galaxy contaminating the UVOT photometry is 50 per cent of the entire galaxy flux. This contribution is removed from the uncorrected magnitude to obtain the flux free of host galaxy contamination. The galactic extinction is further corrected using $E(B-V)$ value of 0.291 following Schlafly & Finkbeiner (2011) with mean galactic extinction laws by Cardelli, Clayton & Mathis (1989). The corrected magnitude is converted to flux using zero-point, and flux density conversion factor from Poole et al. (2008) and Roming et al. (2008), respectively.

3 METHODS AND TECHNIQUES

3.1 Power spectral density (PSD)

We compute the periodogram of 10 d binned *Fermi*-LAT light curve (LC) down to 3 h binning to study the temporal variability. Obtained PSD is fitted with a PL model of the form PSD(ν) $\propto \nu^{-k}$, where k and ν are the spectral index and the frequency, respectively. We used the `power spectral response (PSRESP)' method described in Max-Moerbeck et al. (2014) based on Uttley, McHardy & Papadakis (2002) to obtain the best-fitting values of PL parameters. We simulate 1000 LCs having similar flux distribution as the observed (Emmanoulopoulos, McHardy & Papadakis 2013), accounting for the red-noise leakage, and aliasing effects as described in Goyal et al. (2022).

3.2 Bayesian blocks

We use the Bayesian block (BB; Scargle et al. 2013) algorithm to identify optimal flux states given by constant flux segments of varying duration. The *point-measurement* fitness function with a *false-positive rate* of 5 per cent is used to find a change point indicating when the flux state changes to another distinct state (Abeysekara et al. 2017). The average flux between two change points is considered the flux for the BB. The block's flux uncertainty is the average of each point's flux uncertainty weighted by the inverse square of flux uncertainty.

4 RESULTS

The HE (0.1–300 GeV) LC of BL Lac observed during 13 yr has been divided into five states that are marked with vertical dashed lines in Fig. 1(a) with details provided in Table 1 to study flux and spectral behaviour of the source, where a significant increase in flux was seen after MJD 59000. BB analysis showed 94 change points for the 10 d binned LC (Fig. 1a). The PSD analysis on the LC was performed considering different binning from 10 d down to 3 h time-scales on 13-yr-long *Fermi*-LAT data. The results are tabulated in Table 1.

PSDs spectra from 10 d to 3 h are consistent with pink noise with index ∼1 of PL function in the 0.1–300 GeV range. Interestingly, the obtained PSD spectrum is found to be independent of the flux state. The observed consistency in pink noise from 10 d to 3 h time-scales indicates a similar variability process guiding jet variability regardless of the source's flux state. Furthermore, the variability behaviour of individual flaring activity in the flare S5 has been investigated using multiwaveband LCs from *Swift*-XRT and *Fermi*-LAT.

We study the spectral evolution for four activity regions in S5: (1) S5-1: MJD 59120–59140, (2) S5-2: MJD 59329–59340, (3) S5-3: MJD 59400–59410, and (4) S5-4: MJD 59420–59440 highlighted in Fig. 1(c). The choice of the activity regions is based on the availability of dense X-ray data covering the different flux states of corresponding

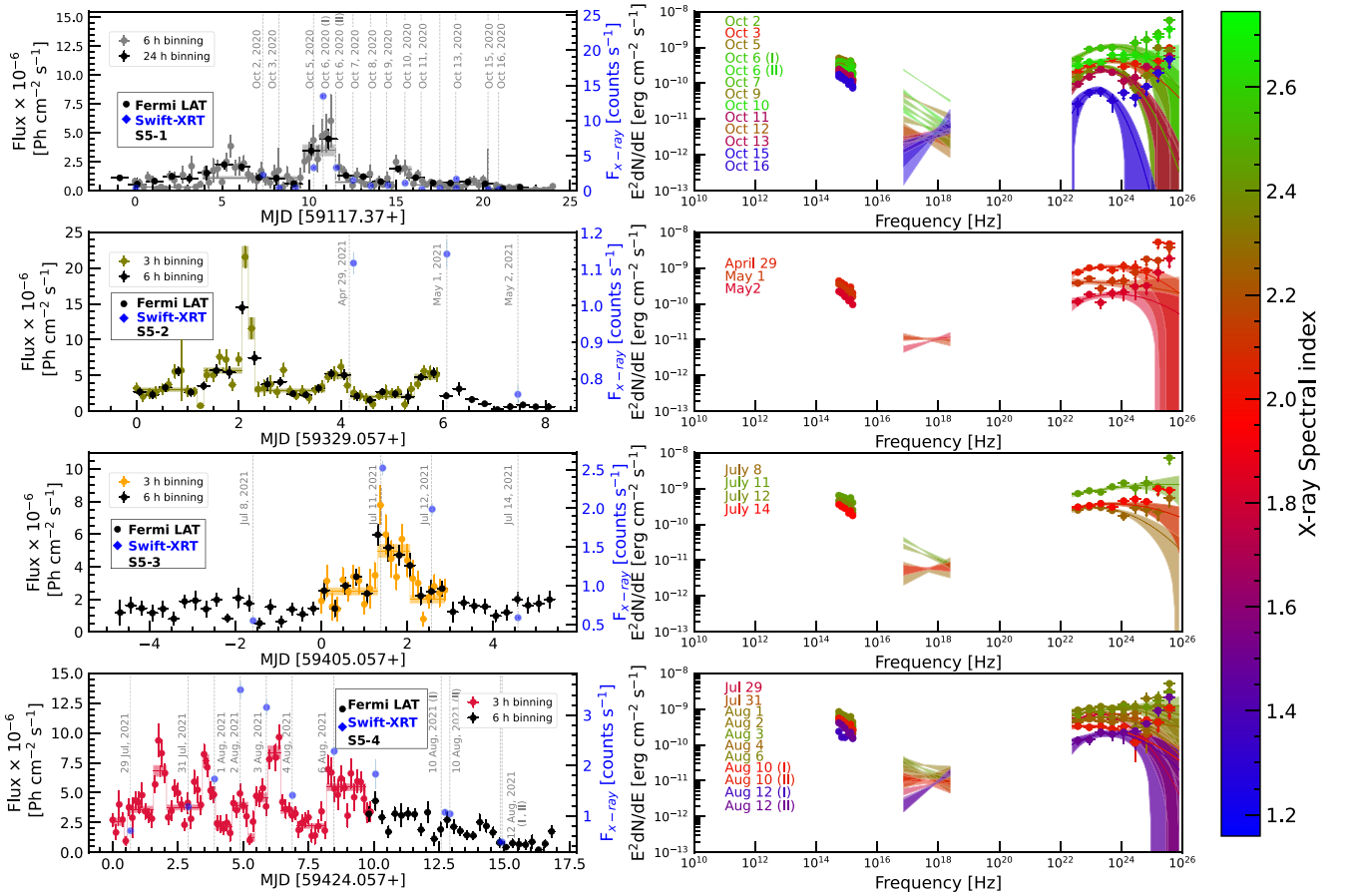

Figure 2. (Left) The *Fermi*-LAT LC of periods highlighted in Figs 1(c) and (d). The *Swift*-XRT LC is plotted on twin axis in blue. Vertical dashed lines represent the times when the MWL SED is studied (right) for the chosen period.

Table 1. PSD results.

Flux state[1]	Time period[2] (d)	T_{obs}[3] (d)	$N_{TS>9}/N_{tot}$[4]	ΔT_{min}[5] (d)	ΔT_{max}[6] (d)	T_{mean}[7] (d)	$\alpha \pm \alpha_{err}$[8]	p_β[9]	$F_{var} \pm \Delta F_{var}$[10]
State 1 (S1)	MJD 54683–55692	1010	93/101	10	20	10.89	0.81 ± 0.37	0.80	0.52 ± 0.03
State 2 (S2)	MJD 55693–56103	410	41/41	10	10	10	0.43 ± 0.66	0.98	0.30 ± 0.02
State 3 (S3)	MJD 56103–57003	900	83/90	10	30	10.86	1.07 ± 0.52	0.65	0.71 ± 0.03
S1 + S2 + S3	MJD 54683–57003	2320	216/231	10	30	10.75	1.17 ± 0.34	0.51	0.69 ± 0.01
State 4 (S4)	MJD 57003–59003	2000	195/195	10	50	10.26	0.94 ± 0.23	0.36	0.42 ± 0.01
State 5 (S5)	MJD 59003–59463	460	46/46	10	10	10	1.24 ± 0.62	0.22	0.64 ± 0.01
State 5 (S5)	MJD 59000–59463	464	447/464	1	4	1.04	1.21 ± 0.21	0.46	0.84 ± 0.01
S5-4	MJD 59420–59440	10	79/79	0.125	0.25	0.13	0.77 ± 0.34	0.14	0.41 ± 0.02
S1 + S2 + S3 + S4 + S5	MJD 54683–59463	4770	457/472	10	50	10.44	1.24 ± 0.29	0.84	1.04 ± 0.01

[1]The flux states based on flux levels. (S1, S2, and S3 are combined to improve the statistics as number of points are less in S2 and S3.)
[2]Time period.
[3]Total exposure.
[4]Fraction of points having TS greater than 9.
[5]Minimum sampling interval in observed LC.
[6]Maximum sampling interval in observed LC.
[7]Mean sampling time interval, i.e. total observation time over a number of data points in that interval.
[8]The PL index for the PL model of PSD analysis.
[9]P value corresponding to the PL model. The PL model is considered a bad fit if $p_\beta \leq 0.1$ as the rejection confidence for such model is >90 per cent.
[10]Fractional variability.

γ-ray activity. State S5-2 is chosen to account for the variability study during the brightest γ-ray activity in the source. The variability time-scales are evaluated using $t_{var} = (t_2 - t_1)\frac{\ln 2}{\ln(F_2/F_1)}$, where F_2 and F_1 are the fluxes at time t_2 and t_1, respectively, and t_{var} is the flux doubling

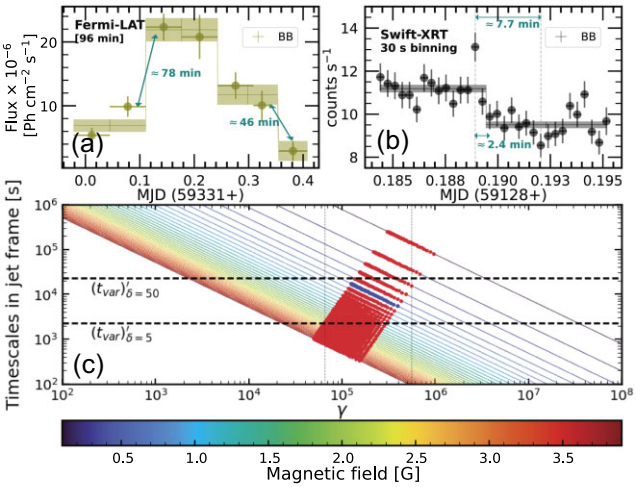

Figure 3. (a) Orbit-binning LC of BL Lac on 2021 April 27, with BBs with a false positive of 5 per cent plotted on top. The flux doubling time-scales at the point of change of the BB is specified. (b) 30 s binned *Swift*-XRT LC for BL Lac corresponding to the brightest X-ray flux observed on 2020 October 6. (c) Synchrotron cooling time-scale corresponding to different electron energies. The red point represents the time-scale for the observed synchrotron emission up to 7.5 keV. The horizontal black line represents the observed time-scales of 7.7 min in jet frame corresponding to Doppler factor between 5 and 50.

and halving time-scales. We checked the shortest variability in X-rays based on the binning of the X-ray LC (10, 15, 20, 25, and 30 s), where we also checked the combination of the LC points. We observed that a wider binning, such as 30 s (adopted in this work), results in a higher significance. The resulting significance quoted in this work is a post-trial significance. The fastest flux variation during S5 was observed on 2020 October 6 by *Swift*-XRT when the variability of $\Delta t_{\rm var} = 7.7 \pm 1.6$ min was detected with 4.8σ confidence (post-trial) and a hint of shorter variability of 2.4 ± 0.9 min was also observed with 2.6σ (post-trial) confidence. These rapid flux changes are also visible as a new BB, see Fig. 3(b). Simultaneous enhancement in the flux is observed in 0.1–300 GeV; however, no evidence of coinciding sub-hour variability is found in the LAT data, mostly due to the limited sensitivity of LAT. Though, an hour-scale variability with a rise time of 78 min on 2021 April 27 and a decay time of 46 min in the falling part of the flare is observed in orbit-binned LC as shown in Fig. 3(a) for state S5-2.

The flux profiles for different states of BL Lac (S1–S5) are estimated using Acciari et al. (2021). The best-fitting model is selected based on a non-overlapping distribution (outside 1σ) of the Akaike information criterion derived from 1000 simulated LCs from a Gaussian, where the mean and the width are the observed flux and the flux uncertainty, respectively. For S3 and S5, lognormal flux distribution is preferred over a Gaussian. The source shows larger variability for S3 and S5 with the values of fractional variability ($F_{\rm var}$; Vaughan et al. 2003) as 0.70 ± 0.03 and 0.64 ± 0.01, respectively. A Gaussian distribution is preferred in S1, where no prominent flare has been observed. The lognormality of flux is also reported in several other blazars in X-rays to VHE γ-rays (Acciari et al. 2021, and references therein) as a consequence of multiplicative processes responsible for the variability. However, Scargle (2020) shows in the general case that multiplicativity is not necessarily needed to obtain an rms–flux correlation and that such correlations have been obtained in specific examples through purely additive processes (Biteau & Giebels 2012).

To study the spectral evolution over 13 yr, the HE LAT spectra of different states are fitted with a log parabola model, parametrized as $\frac{{\rm d}N}{{\rm d}E} = N_\circ \left(\frac{E}{E_b}\right)^{-(\alpha+\beta(\log(E/E_b)))}$ where E_b was fixed to 4FGL catalogue value of 0.7 GeV. The best-fitting spectral parameters are listed in Fig. 1(b). The observed spectral index (α) shows a trend with the increasing flux for the five states; however, the curvature parameter (β) is found to be consistent for each state. In addition, the peak of the HE spectrum shifts to higher energy and is observed at 1 GeV for S5, which is the period with the brightest γ-ray emission. MWL spectral evolution consisting of UV, X-rays, and GeV data is studied during the four activity periods. The epochs with simultaneous observation in *Swift*-XRT and *Fermi*-LAT are chosen based on the BBs covering the *Swift* observation epoch and are shown by vertical dashed lines in Fig. 2. Simultaneous MWL spectral energy distributions (SEDs) are shown on the right-hand side of Fig. 2. The X-ray spectrum is fitted using the absorbed PL model described in Section 2. The source exhibits a softer-when-brighter behaviour in the energy range of 0.2–10 keV in S5.

An evident state change in the X-ray regime is flagged by X-ray emission observed in the second hump of the spectrum during the low-flux state, which evolves into softer X-ray emission via the synchrotron process during the enhanced flux states. This shift is accompanied by hint of shift of the *Fermi*-LAT spectrum to higher energies, as indicated by an apparent shift of the second hump's peak to higher energies and the simultaneous detection of the highest energy photons (HEPs) for the studied state. This effect is especially noticeable in the flare of S5-1 and S5-4. For S5-1, the X-ray emission lies in the rising part of the External Compton (EC) hump from 2020 October 11 to 2020 October 16, in contrast to the observed X-ray emission via synchrotron process from 2020 October 2 to 2020 October 10. The stacked LAT data based on the hardness ratio in the X-rays, softer and harder than -2, result in the peak of LAT spectra at energies from 1.06 ± 0.21 to 1.97 ± 0.05 GeV, indicating that the HE peak shifts to higher energies as the X-ray spectra become harder. For the observed shifted HE peak, the detected HEPs ranged from 7.6 to 53.6 GeV. Similarly, for period S5-4, we observe a transition of X-ray emission via synchrotron process from the EC process as the flux evolves from 2021 July 29 to 2021 August 2. As the flux decays further on 2021 August 12, the spectrum shifts to the second hump. This is visible in the stacked LAT spectrum with a peak at 0.67 ± 0.14 GeV during the periods of hard X-ray spectrum to a shift in peak at 1.84 ± 0.63 GeV during periods of softer X-ray spectrum. The shift is further supported by the detection of HEPs of energies from 71 to 114 GeV during the stacked periods. A hint of a similar shift in S5-3 is highlighted by the detection of HEPs of 172 GeV during 2021 July 11 where the X-ray spectrum lies in the first hump in contrast to the HEPs of 50 GeV during 2021 July 14 where the X-ray spectrum is significantly harder. The spectral shift is shown in Fig. 2.

5 DISCUSSION

BL Lac's flux levels are found to be variable and evolved with time, and its HE spectrum (0.1–300 GeV) can be explained by the log parabola model. The *Fermi*-LAT spectral index (α) gets harder with increasing flux, suggesting fresh or re-accelerated electrons. The spectrum's curvature parameter (β) does not change over 13 yr despite a significant flux change, suggesting a similar influence of external UV photons within or at the edge of the BLR (Poutanen & Stern 2010) on emitted photons in the jet. The observed Lyman Hα lines suggest a weak BLR since from the standard scaling relation,

luminosity $L_{\rm BLR} = 2.5 \times 10^{42}$ erg s^{-1} and $R_{\rm BLR} = 2 \times 10^{16}$ cm (Ghisellini & Tavecchio 2009).

The source is known to be variable in multiple wavebands (Weaver et al. 2020). It was found in high activity in 2020–2021 along with multiple episodes of state change, where X-ray emission shifts from the second to first SED hump. For the first time, minute-scale X-ray variability was found simultaneous with a rare shift of the X-ray emission to the first hump. Moreover, rapid variability and X-ray state change were accompanied by a simultaneous shift of IC peak to the higher energies in activity regions S5-1 and S5-4. Such events are extremely rare in blazars and help constrain emission and particle acceleration models. For the brightest γ-ray flux observed on MJD 59331, the orbit binning reveals a sub-hour variability of 46 min, consistent with observed TeV variability (Arlen et al. 2013). In addition, the correlation of flux–rms versus flux and the dominance of lognormal flux distribution could indicate a multiplicative effect associated with the accretion process (Uttley, McHardy & Vaughan 2005). A minijet-in-jet model can also be a possible explanation for these observations (Biteau & Giebels 2012). Similar PSD for categorized states suggests a similar variability process in the *Fermi* band. The quasi-simultaneous detections of TeV emission, rapid variability, peak shift and X-ray observation at the first hump, and lognormal distribution pose substantial challenges to the shock-in-jet model (Spada et al. 2001).

Corresponding to MJD 59128, during the period of brightest X-ray flux, a minimum variability time of 7.7 ± 1.6 min with a post-trial significance of 4.8σ in X-ray LCs is detected. This corresponds to an emission region located within the BLR at 2.9×10^{15} cm if the emission region covers the entire cross-section of the jet. We also found hints of a shorter variability time-scale of 2.4 ± 0.9 min (2.6σ, post-trial) in 30 s binned *Swift*-XRT data. Similar results are reported by D'Ammando (2021) and Sahakyan & Giommi (2022). A sub-hour variability of 46 ± 24 min is observed on MJD 59331 during the brightest γ-ray state of the source. Pandey & Stalin (2022) hinted at a minute-scale GeV γ-ray variability during this giant γ-ray outburst.

The extension of the synchrotron spectrum up to ~7.5 keV during the high-flux states and hardening of the X-ray spectra during the low-flux state hint at a selective viewing angle during the flare ($\nu_{\rm syn} \propto \gamma^2 B\delta$) or a significant particle acceleration process. The observed 7.5 keV photons provide a signature of the maximum energy of the accelerated electrons. Using synchrotron cooling time-scales, $\tau = \frac{3m_e c}{4\sigma_T \gamma U}$, from equation 12 in Tammi & Duffy (2009) and frequency of emitted synchrotron photons, $\nu_{\rm s} = 4.2 \times 10^6 \gamma^2 B' \frac{\delta}{1+z}$ Hz (Chatterjee et al. 2021), we constrain $\gamma^2 B^{'} \delta = 4.3 \times 10^{11}$ Hz, where $U = U_{\rm mag} = B'^2/8\pi$ for synchrotron losses. The observed time-scale of 7.7 min is translated into the jet frame by using a Doppler factor between 5 and 50. The electron energies responsible for the observed emission of 7.5 keV are found to be $\gamma = 6.5 \times 10^4 - 5.5 \times 10^5$. This limits the magnetic field to be within 0.3–2.2 G (see Fig. 3c).

The shock-in-jet scenario and recollimation shock demand a Doppler factor >100 for the observed luminosity from an emission region corresponding to observed minute-scale variability (Bromberg & Levinson 2009). Such high Doppler factor values contradict the values in kinematic studies of parsec-scale jets and also from magnetohydrodynamical models of the jets (Jorstad et al. 2005).

A possible origin for extended X-ray emission up to 7.5 keV along with observed fast variability and the apparent shift into the second hump could be associated with the preferred alignment of the emission along the line of sight (Meyer, Petropoulou & Christie 2021) through jet-in-jet scenario. Substantial dissipation takes place when reconnection time-scales become equal to expansion time-scales of jet at distances $R_{\rm diss} \simeq \Gamma^2 r_g/\varepsilon$, where ε parametrizes the reconnection rate (Giannios 2013). Thus, the dissipation takes place at $R_{\rm diss} = 4.74 \times 10^{16}$ cm $= 1012\, r_g$ from the central engine, close to the outer boundary of BLR. At the sight of reconnection, magnetic energy is transferred to the particles and results in plasmoid formation (Morris, Potter & Cotter 2019). We expect an enhanced emission and a shift in SED to the higher energies due to Doppler enhancement caused by selective orientation of plasmoid in observer's line of sight. However, when the source fades back to the low state, post-flare, or when the plasmoid is no longer in line of sight, the Doppler boost fades away, and the SED shifts to lower energies.

Considering the jet aligned in line of sight, $\Gamma_{\rm j} = 10$, we compute the Doppler factor of a large plasmoid to be $\delta_{\rm p} = 40$. The emission from the entire reconnection region results in envelope emission, which is significantly lower than the emission from the minijets specifically aligned in the observer's direction. The characteristic size $l^{'}$ is estimated from the envelope time-scale $t_{\rm env}$ as $l' = t_{\rm env}\Gamma_{\rm j}\varepsilon c \sim 5.1 \times 10^{15}$ cm. The plasmoid responsible for the minute-scale flare grows up to 10 per cent ($f = 0.1$) of the reconnection region. The rise/decay time of the minute-scale flare on top of the envelope emission is given by $t_{\rm flare} = f l'/\delta_{\rm p} c \sim 425$ s. Total envelope and plasmoid luminosities that are responsible for envelope and fast-flare emission, respectively, in the jet-in-jet model can be expressed as $L_{\rm env} = 2\Gamma_{\rm j}^2 \delta_{\rm p}^2 l'^2 U_{\rm j}^{'} \varepsilon c$ erg s^{-1} and $L_{\rm P} = 4\pi f^2 l'^2 U_{\rm p}^{''} c \delta_{\rm p}^4$ erg s^{-1}, respectively. Here, ε is the reconnection rate, $U_{\rm j}^{'}$ is the energy density at the dissipation zone in the comoving frame of the jet, and $U_{\rm p}^{''}$ is the energy density of the plasmoid in its comoving frame. We use $U_{\rm j}^{'} = U_{\rm p}^{''}/2$ as in Giannios (2013). The isotropic envelope and plasmoid luminosity are found to be $L_{\rm env} = 3.6 \times 10^{44}$ erg s^{-1} and $L_{\rm p} = 7.2 \times 10^{45}$ erg s^{-1} (for $B' = 0.6$ G), respectively. For such a magnetic field, electron energies for the observed cooling time-scales are within $1.2 \times 10^5 - 4 \times 10^5$.

We conclude that the SED variations and their time-scales reported are in line with a scenario that involves a flaring component and a steady component. Magnetic reconnection gives rise to impulsive particle acceleration in minijets associated with a stochastic flaring component. Growing modes of kink instability can lead to magnetic reconnection beyond the edge of the BLR out to the parsec scale. Such kink instabilities have been located by Jorstad et al. (2022) beyond 5 pc fuelling observed optical activity and cospatial γ-ray emission through synchrotron self-Compton. Close to the edge of the BLR, the SED is dominated by IC scattering by external optical BLR photons (e.g. MAGIC Collaboration 2019).

ACKNOWLEDGEMENTS

SA acknowledges Arti Goyal for useful discussion on manuscript. We thank the referee, Jonathan Biteau, for constructive feedback during the review process. BB and MB acknowledge financial support from MUR (PRIN 2017 grant 20179ZF5KS): The new frontier of Multi-Messenger Astrophysics : follow-up of electromagnetic transient counterparts of gravitational wave sources.

DATA AVAILABILITY

The data used in this letter will be shared upon reasonable request.

REFERENCES

Abdo A. A. et al., 2011, ApJ, 730, 101
Abeysekara A. U. et al., 2017, ApJ, 841, 100

Abeysekara A. U. et al., 2018, ApJ, 856, 95
Acciari V. A. et al., 2021, MNRAS, 504, 1427
Ackermann M. et al., 2011, ApJ, 743, 171
Aleksić J. et al., 2014, Science, 346, 1080
Arlen T. et al., 2013, ApJ, 762, 92
Banasiński P., Bednarek W., Sitarek J., 2016, MNRAS, 463, L26
Biteau J., Giebels B., 2012, A&A, 548, A123
Bromberg O., Levinson A., 2009, ApJ, 699, 1274
Cardelli J. A., Clayton G. C., Mathis J. S., 1989, ApJ, 345, 245
Chatterjee R. et al., 2021, preprint (arXiv:2102.00919)
Corbett E. A., Robinson A., Axon D. J., Hough J. H., Jeffries R. D., Thurston M. R., Young S., 1996, MNRAS, 281, 737
D'Ammando F., 2021, MNRAS, 509, 52
Emmanoulopoulos D., McHardy I. M., Papadakis I. E., 2013, MNRAS, 433, 907
Ghisellini G., Tavecchio F., 2009, MNRAS, 397, 985
Giannios D., 2013, MNRAS, 431, 355
Giannios D., Uzdensky D. A., Begelman M. C., 2009, MNRAS, 395, L29
Goyal A. et al., 2022, ApJ, 927, 214
Jorstad S. G. et al., 2005, AJ, 130, 1418
Jorstad S. G. et al., 2022, Nature, 609, 265
MAGIC Collaboration, 2019, A&A, 623, A175
Max-Moerbeck W., Richards J. L., Hovatta T., Pavlidou V., Pearson T. J., Readhead A. C. S., 2014, MNRAS, 445, 437
Meyer M., Petropoulou M., Christie I. M., 2021, ApJ, 912, 40
Miller J. S., French H. B., Hawley S. A., 1978, ApJ, 219, L85
Morris P. J., Potter W. J., Cotter G., 2019, MNRAS, 486, 1548
Nilsson K. et al., 2018, A&A, 620, A185
Pandey A., Stalin C. S., 2022, A&A, 668, A152
Poole T. S. et al., 2008, MNRAS, 383, 627
Poutanen J., Stern B., 2010, ApJ, 717, L118
Raiteri C. M. et al., 2013, MNRAS, 436, 1530
Roming P. W. A. et al., 2008, ApJ, 690, 163
Sahakyan N., Giommi P., 2022, MNRAS, 513, 4645
Scargle J. D., 2020, ApJ, 895, 90
Scargle J. D., Norris J. P., Jackson B., Chiang J., 2013, ApJ, 764, 167
Schlafly E. F., Finkbeiner D. P., 2011, ApJ, 737, 103
Shukla A., Mannheim K., 2020, Nat. Commun., 11, 4176
Spada M., Ghisellini G., Lazzati D., Celotti A., 2001, MNRAS, 325, 1559
Stroh M. C., Falcone A. D., 2013, ApJS, 207, 28
Tammi J., Duffy P., 2009, MNRAS, 393, 1063
Tavecchio F., Becerra-Gonzalez J., Ghisellini G., Stamerra A., Bonnoli G., Foschini L., Maraschi L., 2011, A&A, 534, A86
Uttley P., McHardy I. M., Papadakis I. E., 2002, MNRAS, 332, 231
Uttley P., McHardy I. M., Vaughan S., 2005, MNRAS, 359, 345
Vaughan S., Edelson R., Warwick R. S., Uttley P., 2003, MNRAS, 345, 1271
Weaver Z. R. et al., 2020, ApJ, 900, 137
Wood M., Caputo R., Charles E., Di Mauro M., Magill J., Perkins J. S., 2017, Proceedings of 35th International Cosmic Ray Conference PoS (ICRC2017), 301, 824

This paper has been typeset from a TEX/LATEX file prepared by the author.